Ultrasonics 95 (2019) 95–103

Contents lists available at ScienceDirect

Ultrasonics

journal homepage: www.elsevier.com/locate/ultras

# Novel mesoporous $MnO_2/SnO_2$ nanomaterials synthesized by ultrasonic-assisted co-precipitation method and their application in the catalytic decomposition of hydrogen peroxide

Hala R. Mahmoud*, Sahar A. El-Molla, Mona A. Naghmash

*Department of Chemistry, Faculty of Education, Ain Shams University, Roxy 11757, Cairo, Egypt*

ARTICLE INFO

*Keywords:*
Ultrasonic co-precipitation
$MnO_2/SnO_2$
Ultrasonic power and time effects
Nanomaterials
Catalytic decomposition of $H_2O_2$

ABSTRACT

Novel mesoporous $MnO_2/SnO_2$ catalysts were successfully synthesized via traditional and ultrasonic co-precipitation methods. Moreover, their catalytic efficiencies were evaluated in decomposition of hydrogen peroxide ($H_2O_2$). Interestingly, it was found that the mixing of $MnO_2$ with $SnO_2$ catalyst led to a significant improvement in their catalytic efficiencies compared with single oxides catalysts. However, the influence of ultrasonic power and irradiation time on $MnO_2/SnO_2$ nanomaterials were compared to get optimum synthetic condition. Subsequently, the catalysts were characterized by X-ray diffraction (XRD), $N_2$ adsorption-desorption analysis and high-resolution transmission electron microscopy (HR-TEM). Results represented that the effect of ultrasonic power and irradiation time on $MnO_2/SnO_2$ catalysts exerted a great influence on the BET surface area and average particle diameter. Furthermore, the results showed that the best catalytic efficiency was obtained for the mesoporous $MnO_2/SnO_2$ catalyst which is sonicated at power of 60% for 30 min as optimum conditions. Finally, the outcomes appeared that the catalysts synthesized by ultrasonic co-precipitation method were more efficient than those synthesized by traditional co-precipitation in catalyzing $H_2O_2$ decomposition.

## 1. Introduction

In former little years, huge efforts were devoted to the area of nanotechnology [1–3] predominately on the metal oxide nanoparticles due to their comparatively high chemical efficiency in addition specificity of interaction. These nanomaterials have many various properties such as high surface area, adjustable size and shape of pores, several different structures and compositions in comparison to their bulk equivalents [4,5]. Among all the nanomaterials, the transition metal oxides in the nanoscale were noticeable candidates from a scientific and technological view point [6,7]. Further, transition metal oxides can offer individual advantages which make them the most multilateral category of substances with properties covering all sides of solid state and materials science [8]. Manganese oxides are one of the most favorable transition metal oxide catalysts because of their good redox properties and powerful oxygen storage/release capacity [9]. There are many forms of manganese oxides MnO, $Mn_3O_4$, $Mn_2O_3$ and $MnO_2$ [10]. Generally, $MnO_2$ was found in nature as the form of pyrolusite mineral [11]. $MnO_2$ was thermally stable until a temperature around 500 °C, above which thermal decomposition occur and $MnO_2$ converts to $Mn_2O_3$ [12,13]. $MnO_2$ was vastly utilized in different industrial fields such as sensors, in dry cell batteries as the primary component of the cathode mixture, catalyst for ethylene hydrogenation, a great potential in environmental cleanup due to its high catalytic activity, low toxicity and thermal stability [12–14]. Among various metal oxide semiconductors, tin dioxide ($SnO_2$), was considered as one of the smart substances because of its superior stability, its wide band gap, its high surface area, its porous nature, excellent optical and electrical properties, nontoxicity and low cost which are appropriate to apply $SnO_2$ in many fields [15,16]. It possesses a high position in the fields of gas-sensing, energy storage, transparent conducting electrodes, antireflection coatings [17], and catalysis [18]. The catalytic properties of metal oxides were strongly affected by the method of preparation, therefore various methods were used to prepare metal oxides nanomaterials such as co-precipitation [19], impregnation [20], electrochemical reductions [21], thermal decomposition [22] microwave-assisted [23] and hydrothermal [24]. Co-precipitation as a traditional method normally used for synthesis of metal oxides since it is easy, cheap and performed without high temperature or pressure. This method affected by pH of the medium, concentration of the starting materials and precipitating reagents [25]. Through the quick progress of nanoscience and nanotechnology, it was necessary to apply new methods for nanomaterials

* Corresponding author.
*E-mail address:* halarashaad@edu.asu.edu.eg (H.R. Mahmoud).

https://doi.org/10.1016/j.ultras.2019.03.011
Received 20 October 2018; Received in revised form 13 February 2019; Accepted 13 March 2019
Available online 15 March 2019
0041-624X/ 

synthesis such as ultrasonic irradiation, microwave heating and mechanochemical techniques. Ultrasonic technology is an environmentally friendly method for preparing catalysts and can minimize the exhaustion of chemical reagents and energy [26,27]. The physicochemical influences of ultrasonic cavitation can accelerate the scattering of active phase on the support surface, thus gaining catalysts with good dispersion on the surface and in nano-scale [26,28]. Hydrogen peroxide ($H_2O_2$) is an environmentally friendly oxidant because its oxidation by-products were oxygen and water, and thus it was generally used in wastewater treatment, detergent, petrochemical and paper industries [29–31]. Furthermore, the decomposition of $H_2O_2$ has been widely investigated as a probe reaction for redox efficiency of both homogeneous and heterogeneous catalysts [29]. In the past, the reaction has been under scanning of space agencies as a possible major ingredient in several forms of propulsion systems regarding space technologies [32]. It has been reported that active metal catalysts became unable to resist the setting-up of high temperature regimes in the adiabatic thrusters frequently applied [33,34]. Thus, thermally very stable, although less active, substitutional metal oxide catalysts were examined [34].

To the best of our knowledge, the influence of ultrasonic power and irradiation time on mesoporous $MnO_2/SnO_2$ catalysts for catalytic decomposition of $H_2O_2$ has not been reported. As well, the $SnO_2$, $MnO_2$ and $MnO_2/SnO_2$ nanomaterials were synthesized by traditional co-precipitation method for comparison. Furthermore, the influence of ultrasonic power and irradiation time on $MnO_2/SnO_2$ nanomaterials were compared to get optimum synthetic condition. The prepared catalysts were characterized by various physicochemical techniques such as X-ray diffraction (XRD), $N_2$ adsorption-desorption analysis and high-resolution transmission electron microscopy (HR-TEM). Also, their catalytic activities were investigated in decomposition of $H_2O_2$.

## 2. Experimental

### 2.1. Materials

All raw materials in this study were of analytical grade and used without further purification. Tin chloride ($SnCl_2{\cdot}H_2O$), manganese nitrate ($Mn(NO_3)_2{\cdot}4H_2O$), ammonium hydroxide ($NH_4OH$, 28%) and hydrogen peroxide ($H_2O_2$, 33%).

### 2.2. Preparation of single metal oxides

Manganese nitrate ($Mn(NO_3)_2{\cdot}4H_2O$) and tin chloride ($SnCl_2{\cdot}2H_2O$) were used as the starting precursors to prepare 0.5 M $MnO_2$ and 0.5 M $SnO_2$ nanomaterials as single oxides by precipitation method. In a typical preparation, certain amounts of ($Mn(NO_3)_2{\cdot}4H_2O$) and ($SnCl_2{\cdot}2H_2O$) were dissolved separately in 250 mL of bi-distilled water under magnetic stirring at a temperature of 80 °C for 10 min then 28% $NH_4OH$ was added drop-wise into each solution until pH = 8. The obtained precipitates were filtered, washed with bi-distilled water several times until free from anion impurities then dried at 100 °C overnight. Finally, the prepared powders were calcined in a muffle furnace at 500 °C for 3 h. Thus, to represent simply; the final products were denoted as $MnO_P$ and $SnO_P$.

### 2.3. Preparation of mixed metal oxides

The $MnO_2/SnO_2$ nanomaterials were synthesized by traditional co-precipitation method with equal molar ratio. In brief, the required amounts of manganese nitrate and tin chloride were dissolved separately in bi-distilled water then were mixed together with magnetic stirring at 80 °C. Where after, 28% ammonia solution was slowly added to the above solution under continuous stirring until pH = 8. Finally, the precipitate was filtered, washed with bi-distilled water several times, dried at 100 °C overnight and then calcined at 500 °C for 3 h. The obtained nanomaterial was denoted as $MnSnO_{CP}$.

### 2.4. Preparation of $MnO_2/SnO_2$ nanomaterials by ultrasonic co-precipitation method

The preparation was identical to that as afore said in Section 2.3, where instead of stirring the mixture using magnetic stirrer, the nanomaterials were sonicated after adding ammonia solution using UP50H sonication probe (30 kHz, 50 W). In this study, two parameters were investigated, one in which the samples were sonicated at room temperature with different power levels (20%, 40%, 60%, 80% and 100%) for 30 min. In the other, the samples were sonicated at power of 60% with different ultrasonic time (15, 20, 30, 40 and 60 min). Finally, the nanomaterials were washed, dried in oven at 100 °C, and then calcined at 500 °C for 3 h. The prepared nanomaterials were denoted as $MnSnO_{US(x)y}$, in which "X" and "Y" represented the sonication power and time, respectively. This preparation method was named as "US" method. For example, the nanomaterial which denoted as $MnSnO_{US(20\%)30}$ where (20%) refers to the sonication power and 30 refers to the sonication time for 30 min. For comparison, the $SnO_2$ and $MnO_2$ were also prepared by ultrasonic method at power of 60% for 30 min and donated as $SnO_{US(60\%)30}$ and $MnO_{US(60\%)30}$.

### 2.5. Catalyst characterization

X-ray diffraction (XRD) patterns were obtained using a Bruker Axs D8 Advance X-ray diffractometer (Germany) using CuKα1 irradiation (λ = 0.15404 nm) at a scan rate of 2° in 2θ/min. The crystallite size of crystalline phases of prepared catalysts was calculated using Scherrer's equation [35]:

$$D = k\lambda/\beta\cos\theta \quad (1)$$

where D is the crystallite size, k is the Scherrer constant and equal to 0.9, λ is the wavelength of radiation, β is the full width at half maximum (FWHM) of the diffraction peak and θ is the diffraction angle.

Nitrogen sorption experiments were performed at 77 K with a Quantachrome NOVA 3200 automated gas-sorption apparatus model 10 (USA). The samples were pretreated at 200 °C for overnight under vacuum. The surface areas were calculated using the Brunauer–Emmett–Teller (BET) method. The pore volume, $V_p$ was evaluated by converting the volume of nitrogen adsorbed at $P/P_o$ of about 0.99 to the volume of liquid nitrogen per gram of the material. The pore size distribution was calculated from desorption branch of the isotherm by the Barrett, Joyner and Halenda (BJH) method. The morphology of the catalysts was observed by high-resolution transmission electron microscope (HR-TEM) microanalysis system (JEM-2100CX (JEOL)).

### 2.6. Catalytic reaction

The catalytic decomposition of hydrogen peroxide ($H_2O_2$) in presence of the prepared catalysts was determined. 100 mg of catalyst was mixed with (5 mL $H_2O_2$ + 15 mL distilled $H_2O$) and stirred at room temperature (20 °C) for 1 h. After this time, the reaction was stopped by adding ice. The solution was filtrate, the filtrate was titrated with 0.1 N $KMnO_4$ solution under acidic media using $H_2SO_4$ (2 N, 10 mL) at 90 °C. The difference in values of the $KMnO_4$ solution before and after the catalyzed decomposition was determined. A blank test was as well simultaneously carried out without catalyst under the same condition. Percentage of $H_2O_2$ that decomposed by these catalysts were calculated by the following formula

$$\%H_2O_2 \text{ decomposition} = 100 \times (a_o - a_t)/a_o \quad (2)$$

where $a_o$ is the initial concentration of $H_2O_2$ and $a_t$ is the concentration of $H_2O_2$ at time (t).

To evaluate the stability of the catalyst, four consecutive run tests were done after the catalytic decomposition of $H_2O_2$ the solid catalyst was recovered and undergo to following run.

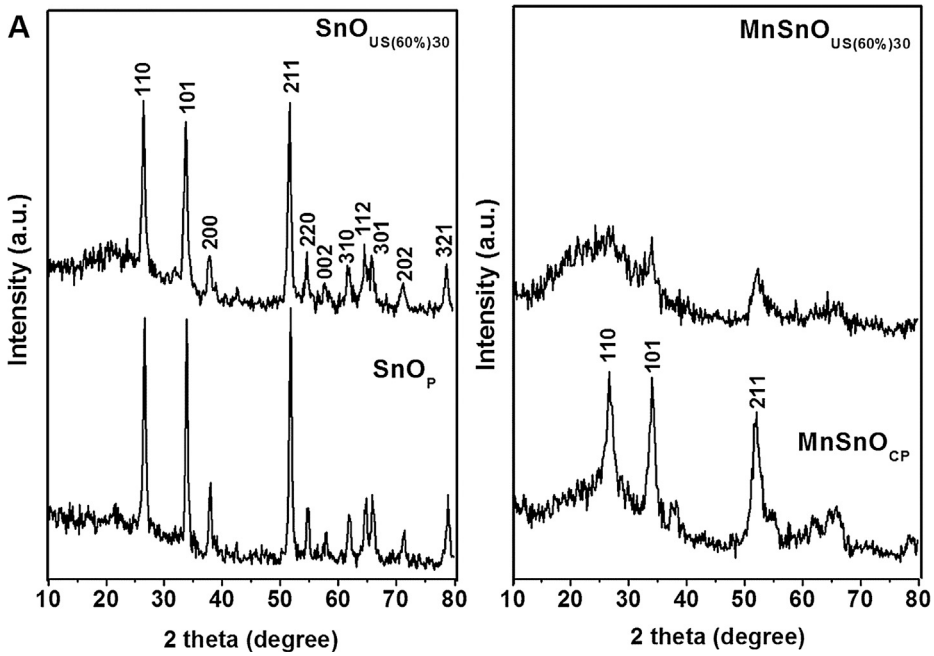


**Fig. 1A.** XRD patterns of $SnO_p$, $SnO_{US(60\%)30}$, $MnSnO_{CP}$ and $MnSnO_{US(60\%)30}$ nanomaterials calcined at 500 °C.

## 3. Results and discussion

### 3.1. X-ray diffraction (XRD) analysis

Fig. 1A depicts the XRD patterns of $SnO_p$, $SnO_{US(60\%)30}$, $MnSnO_{CP}$ and $MnSnO_{US(60\%)30}$ nanomaterials. In the patterns of pure $SnO_p$ and $SnO_{US(60\%)30}$ catalysts, there are intense and sharp diffraction peaks at 2θ = 26.67°, 33.94°, 37.98°, 51.86°, 54.85°, 57.91°, 62.0°, 64.82°, 66.10°, 71.32° and 78.71° which ascribed to (1 1 0), (1 0 1), (2 0 0), (2 1 1), (2 2 0), (0 0 2), (3 1 0), (1 1 2), (3 0 1), (2 0 2) and (3 2 1) lattice planes, respectively. All the diffraction peaks establish the formation of the $SnO_2$ nanoparticles in tetragonal rutile structures (JCPDS No. 41-1445) [36]. As could be seen from Fig. 1A that the pure $SnO_2$ sample prepared by traditional precipitation method had high intense diffraction peaks than those prepared by ultrasonic precipitation method. The average crystallite sizes of $SnO_p$ and $SnO_{US(60\%)30}$ nanomaterials were found to be 29.1 nm and 21.2 nm, respectively. Consequently, the sonication method led to decrease the size of the particles and the crystallinity without any phase variation. This can be explained to the ambiences generated through sonication and facilitating quicker reaction, not permitting the nucleation and crystal development to take place fully [37]. The cavitation influence of ultrasound can create high local energy and micro mixing which acts as a reaction support, which increases the randomness motion of the $SnO_2$ molecules not permitting regular crystal formation. This will decrease the crystal size and crystallinity of synthesized catalyst due to changeable position of molecules in the lattice [37,38]. Furthermore, the pattern of $MnSnO_{CP}$ nanomaterial was exhibited much more broadening diffraction peaks at 2θ = 26.67°, 33.94° and 51.86° after mixing the $SnO_2$ with manganese oxide, which can be indexed to the $SnO_2$ (JCPDS No. 41-1445) as shown in Fig. 1A. Meanwhile, no manganese oxide phase was found in the patterns, indicating that manganese ions could be incorporated into the lattice matrix of $SnO_2$ to form solid solution structure [39]. This can be explained to comparable ionic radii of $Mn^{4+}$ (0.54 Å) and $Mn^{3+}$ (0.65 Å) which smaller than $Sn^{4+}$ (0.69 Å) [40–42]. In addition, the peaks broadening after mixing, implying the lowering in the crystallinity and crystallite sizes of catalysts [40]. Therefore, $MnSnO_{CP}$ sample was appeared as amorphous material. Furthermore, the XRD patterns of $MnSnO_{US(20\%)30}$, $MnSnO_{US(60\%)30}$, $MnSnO_{US(80\%)30}$, $MnSnO_{US(60\%)15}$ and $MnSnO_{US(60\%)60}$ nanomaterials were shown in Fig. 1B. The analysis of those patterns revealed that no diffraction peaks of any phases were detected, indicating that all catalysts prepared by ultrasonic co-precipitation method with different sonication power and times were amorphous materials.

### 3.2. Nitrogen adsorption-desorption analysis

To mark the influence of ultrasonic method on the surface area and pore structures of the synthesized $SnO_2$, $MnO_2$ and $MnO_2/SnO_2$ nanomaterials, nitrogen adsorption-desorption isotherms were investigated and represented in Fig. 2A. The isotherms of $SnO_{US(60\%)30}$, $MnO_{US(60\%)30}$, $MnSnO_{CP}$, $MnSnO_{US(20\%)30}$, $MnSnO_{US(60\%)30}$ and $MnSnO_{US(60\%)60}$ catalysts show type IV curves with H3 hysteresis loops which were characteristics of mesoporous materials [43], having a slit-shaped pores structures as seen in Fig. 2A [44,45]. Moreover, the BJH pore size distributions of all nanomaterials were showed distributions in the low mesoporous region with average pore diameters around 5 nm as represented in Fig. 2B. The BET surface area, pore volume and pore size of the synthesized catalysts were summarized in Table 1. It has been reported that the BET surface area of $SnO_2$ and $MnO_2$ samples prepared by traditional precipitation method was 28.0 $m^2/g$ and 23.2 $m^2/g$, respectively [46,47]. Furthermore, in our study, the single oxides prepared by ultrasonic precipitation ($SnO_{US(60\%)30}$) and ($MnO_{US(60\%)30}$) had BET surface area of 30.6 $m^2/g$ and 32.1 $m^2/g$, respectively. In addition, the specific surface area of $MnO_2/SnO_2$ catalysts either prepared by traditional or ultrasonic co-precipitation method were higher than that of single oxides with about 33%, 61% compared to $SnO_2$ and 44% and 59% compared to $MnO_2$, respectively. Thus, the mixing of $MnO_2$ with $SnO_2$ catalyst led to a significant improvement of its specific surface area due to lowering the crystal size of mixed oxide [48]. Interestingly, the BET surface area and pore volume of $MnO_2/SnO_2$ catalysts prepared by ultrasonic co-precipitation at different sonication power and time were significantly higher than that catalyst made by traditional co-precipitation. In other words, the surface areas of $MnSnO_{US(20\%)30}$, $MnSnO_{US(60\%)30}$ and $MnSnO_{US(60\%)60}$ catalysts were 40%, 47% and 34%, more compared to $MnSnO_{CP}$ catalyst, respectively. The reason for enormous variation might be attributed to mechanical effect of ultrasound [49]. Where, micro-jet and shock waves created by ultrasound broke the catalyst particles to smaller particles [28]. It was

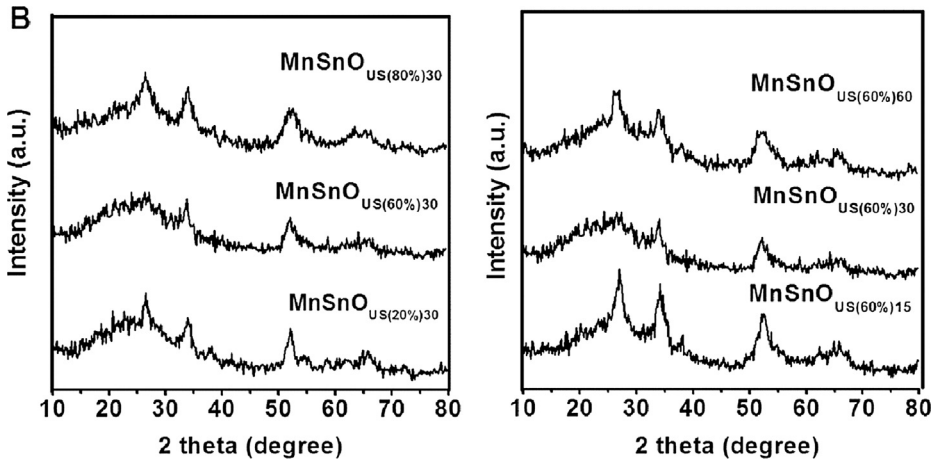


**Fig. 1B.** XRD patterns of $MnSnO_{US(20\%)30}$, $MnSnO_{US(60\%)30}$, $MnSnO_{US(80\%)30}$, $MnSnO_{US(60\%)15}$ and $MnSnO_{US(60\%)60}$ nanomaterials calcined at 500 °C.

noteworthy that increasing the sonication power from 20% to 60% increases the BET surface area of catalyst from 69.2 $m^2$/g to 78.6 $m^2$/g, because increasing the ultrasonic power increases the temperature which reduces the nucleation of the particles [50]. On other hand, increasing the sonication time from 30 min to 60 min decreases the BET surface area from 78.6 $m^2$/g to 60.2 $m^2$/g, this can be explained to re-agglomeration of particles after increasing ultrasonic time [51]. Finally, the $MnSnO_{US(60\%)30}$ catalyst obtained under the best preparation conditions (sonication power = 60% and ultrasonic time = 30 min) had the highest BET surface area and pore volume, which makes it attractive in the catalytic performance.

### 3.3. HR-TEM analysis

To study the morphological change due to ultrasonication effect, HR-TEM analysis was investigated on $MnSnO_{CP}$, $MnSnO_{US(60\%)30}$ and $MnSnO_{US(60\%)60}$ catalysts and the images were presented in Fig. 3. The HR-TEM images of catalysts were prepared by traditional and ultrasonic co-precipitation methods showed spherical like structure with particles agglomerated. Moreover, the average pore diameter was about 32.0 nm, 5.2 nm and 9.5 nm for $MnSnO_{CP}$, $MnSnO_{US(60\%)30}$ and $MnSnO_{US(60\%)60}$ nanomaterials, respectively. Thus, the catalyst particles size showed that sonication method produced obvious smaller grains with weak agglomeration. This because of the shock waves of ultrasound led to break the catalyst particles to smaller one [28]. Further, the cavitation influence of ultrasound can create high temperatures and pressures [52]. The high temperature and pressure break the chemical bonds facilely and make the reactions to carry out. Since collapsing of cavitation bubble occurs in lower than a nanosecond, the temperature decreases speedily, this stops the agglomeration of particles [28]. On other hand, it was found that increasing the sonication time from 30 min to 60 min increases the particles size and degree of agglomeration; this can be attributed to re-agglomeration of particles after increasing the ultrasonic time [51]. Furthermore, in this study found that the ultrasonication for 30 min showed the lowest particles size and agglomeration. This analysis was confirmed by the following BET results. Finally, the ultrasonic irradiation plays vital role in the catalytic performance.

### 3.4. Catalytic decomposition of hydrogen peroxide ($H_2O_2$)

#### 3.4.1. Effect of $MnO_2$ mixing with $SnO_2$ catalyst

The catalytic activity experiments at room temperature (20 °C) were done to evaluate the efficiency of $SnO_2$, $MnO_2$ and $MnO_2/SnO_2$ nanomaterials to act as catalysts in $H_2O_2$ decomposition. Fig. 4 represented the catalytic activity in absence the catalyst and in the presence of $SnO_P$, $MnO_P$, $MnSnO_{CP}$, $SnO_{US(60\%)30}$, $MnO_{US(60\%)30}$, $MnSnO_{US(60\%)30}$. The decomposition of $H_2O_2$ without catalyst which obtained under the same conditions was negligible, since it was about 5.1%. Furthermore, the catalytic efficiency for $H_2O_2$ decomposition of mixed oxides $MnO_2/SnO_2$ either prepared by traditional or ultrasonic co-precipitation method was greater than that of single oxides. In addition, the $SnO_{US(60\%)30}$, $MnO_{US(60\%)30}$ and $MnSnO_{US(60\%)30}$ were more active catalysts in comparison to the $SnO_P$, $MnO_P$, and $MnSnO_{CP}$ in catalyzing $H_2O_2$ decomposition. In other words, the percentage of $H_2O_2$ that decomposed using $SnO_P$, $MnO_P$, $MnSnO_{CP}$, $SnO_{US(60\%)30}$, $MnO_{US(60\%)30}$ and $MnSnO_{US(60\%)30}$ was found to be 25.0%, 30.0%, 37.5%, 45.6%, 50.5%, and 84.4%, respectively. Thus, the results showed that the prepared catalysts by ultrasonic co-precipitation method were more efficient than those prepared by traditional co-precipitation in catalyzing $H_2O_2$ decomposition.

The efficiency of ultrasound chemical reactions was generally due to the cavitation of ultrasound [53]. When a certain intensity of ultrasonic irradiation was applied to a liquid, many teeny bubbles were produced. These teeny bubbles cause a group of physical and chemical changes through their formation, vibration, growth, and constriction to collapse. This influence is called cavitation [54]. When the cavitation bubble collapses, a big quantity of energy was emitted inside and around the cavitation bubble [55] which enhances the decomposition of $H_2O_2$.

It has reported that $H_2O_2$ decomposition involves the electron transport from the catalyst surface to the $H_2O_2$ molecule [31]. The higher catalytic activity of the mixed catalysts for $H_2O_2$ decomposition, compared to the single one, was thus interpreted by the presence of coupled ions in different oxidation states facilitates d-d electron exchange interactions [56]. The ion-couples expose at the surface of mixed oxides possibly were $Sn^{2+}$-$Mn^{4+}$, $Mn^{3+}$-$Sn^{4+}$, $Mn^{2+}$-$Sn^{4+}$, $Mn^{3+}$-$Mn^{4+}$, $Mn^{2+}$-$Mn^{3+}$ and/or $Sn^{2+}$-$Sn^{4+}$ [57–61] which produce the optimal electron-mobile environment for surface redox catalysis [62]. It has been reported that the multiple oxidation states of Mn element ($Mn^{4+}$, $Mn^{3+}$ and $Mn^{2+}$) in manganese dioxide ($MnO_2$) promote its activity in heterogeneous catalysis [28,63].

#### 3.4.2. Effect of sonication power

It was of interest to study the effect of different sonication power from 20% to 100% on the decomposition of hydrogen peroxide at 20 °C as shown in Fig. 5. Further, it was observed that the catalytic efficiency of $MnO_2/SnO_2$ increases by increasing the sonication power reached to a maximum at 60% then decreases by increasing the sonication power. In other speech, the percentage of $H_2O_2$ that decomposed using $MnSnO_{US(20\%)30}$, $MnSnO_{US(40\%)30}$, $MnSnO_{US(60\%)30}$, $MnSnO_{US(80\%)30}$ and $MnSnO_{US(100\%)30}$ was found to be 50.0%, 75.0%, 84.4%,75.0% and 46.9%, respectively. So, the $MnSnO_{US(60\%)30}$ catalyst was the most

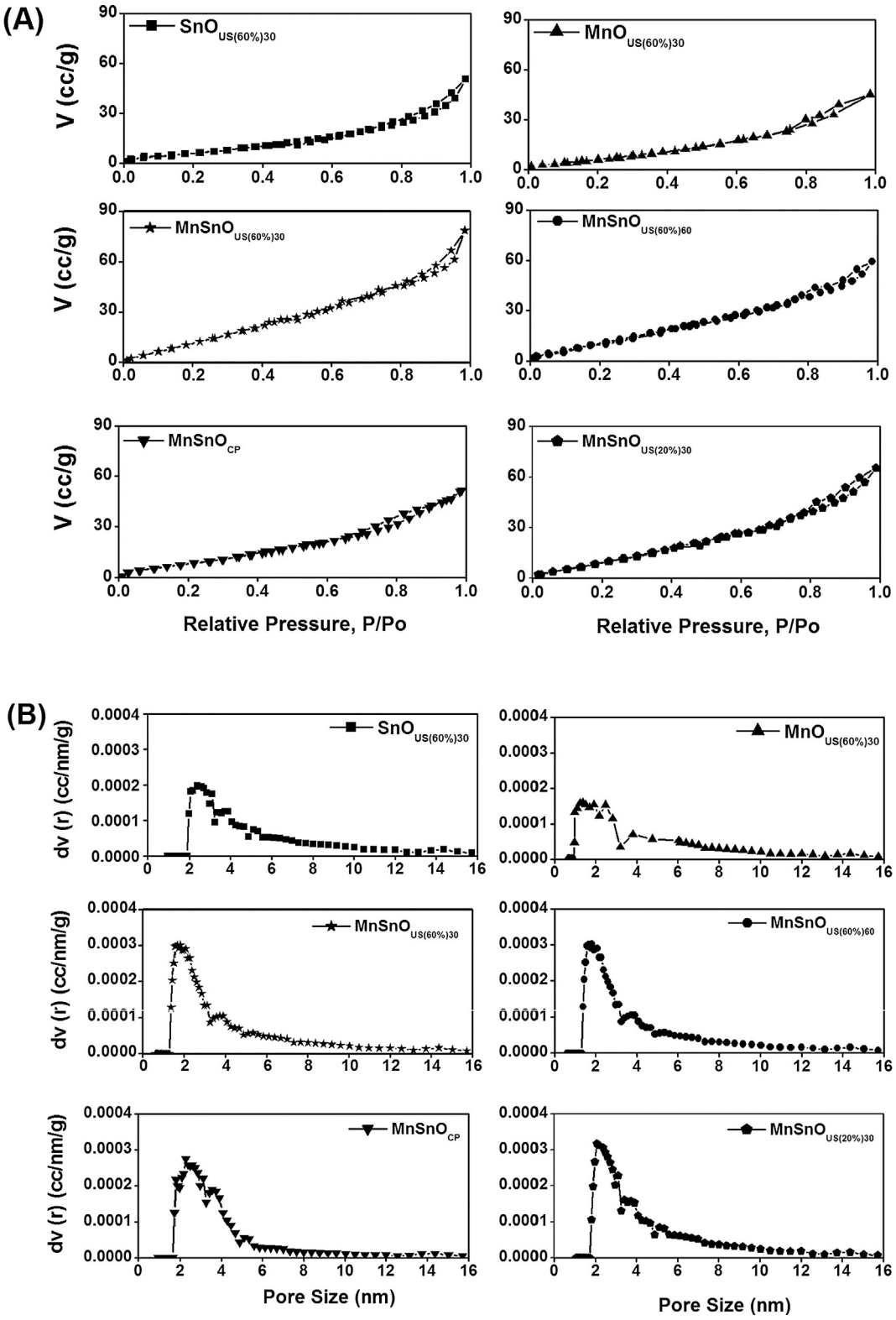


**Fig. 2.** (A) Nitrogen adsorption–desorption isotherms and (B) Pore size distribution of $SnO_{US(60\%)30}$, $MnO_{US(60\%)30}$, $MnSnO_{CP}$, $MnSnO_{US(20\%)30}$, $MnSnO_{US(60\%)30}$ and $MnSnO_{US(60\%)60}$ catalysts calcined at 500 °C.

active one which catalyzes $H_2O_2$ decomposition while the $MnSnO_{US(100\%)30}$ was the lowest active catalyst. This could be attributed to the highest BET surface area and the lowest particles size which resulting in a larger number of electrons donating active sites available for $H_2O_2$ decomposition.

Additionally, as the intensity of the ultrasonic irradiation increases, the cavitation bubble collapses more sharply, producing higher temperature and pressure [64] which enhances the decomposition of $H_2O_2$. It has been reported that different ultrasonic reactors had their better ultrasound intensity, and the activity decreases with increasing ultrasound intensity when the sound is stronger than the optimal value [53]. This could be explained as a following: (i) higher ultrasound intensity

**Table 1**
BET surface area, pore volume and pore diameter of $SnO_2$, $MnO_2$ and $MnO_2$/$SnO_2$ nanomaterials calcined at 500 °C.

| Catalyst | $S_{BET}$ ($m^2$/g) | $V_P$ ($cm^3$/g)[a] | Pore diameter (nm)[b] |
|---|---|---|---|
| $SnO_{US(60\%)30}$ | 30.6 | 0.076 | 4.5 |
| $MnO_{US(60\%)30}$ | 32.1 | 0.074 | 4.5 |
| $MnSnO_{CP}$ | 41.7 | 0.077 | 4.5 |
| $MnSnO_{US(20\%)30}$ | 69.2 | 0.099 | 4.5 |
| $MnSnO_{US(60\%)30}$ | 78.6 | 0.118 | 4.2 |
| $MnSnO_{US(60\%)60}$ | 60.2 | 0.089 | 3.6 |

[a] Pore volume determined around saturation pressure.
[b] Calculated by BJH method.

can increases the cavitation bubbles in the solution, which led to the diffusion of ultrasonic irradiation and reduction of some energy; (ii) as well the increase in the ultrasound intensity makes the cavitation bubble in the negative sound pressure phase expand very large to form a sonic armor which reduces the energy of the ultrasound area available to the system [53].

### 3.4.3. Effect of sonication time

The $MnSnO_{US(60\%)30}$ catalyst which exhibited the highest catalytic efficiency for $H_2O_2$ decomposition at 20 °C was selected for another study, namely to study the effect of the sonication time on the $H_2O_2$ decomposition. The catalytic efficiency of the catalyst increased as the sonication time was increased reached to a maximum at 30 min then decreased as shown in Fig. 6. In other terms, the percentage of $H_2O_2$ that decomposed by $MnSnO_{US(60\%)15}$, $MnSnO_{US(60\%)20}$, $MnSnO_{US(60\%)30}$, $MnSnO_{US(60\%)40}$ and $MnSnO_{US(60\%)60}$ was found to be 62.5%, 73.8%, 84.4%, 62.5% and 46.9%, respectively. Hence, the catalyst which sonicated for 30 min exhibited the highest catalytic efficiency nevertheless the catalyst sonicated for 60 min showed the lowest efficiency. It was reported that [65,66] with increasing the ultrasonic time, the nanoparticles became more homogeneous. However, further increasing the ultrasonic time resulted in re-agglomeration.

Finally, the results confirmed that the best catalytic efficiency was obtained for the mesoporous $MnO_2$/$SnO_2$ catalyst which sonicated at power of 60% for 30 min as optimum conditions in the preparation method. Because of the highest surface area and the lowest particles size which can be produced a larger number of electrons donating active sites available for $H_2O_2$ decomposition.

### 3.4.4. Kinetic study

The decomposition of hydrogen peroxide was generally assumed to be a pseudo first order reaction. To follow the kinetics, the most active catalyst in $H_2O_2$ decomposition ($MnSnO_{US(60\%)30}$) was selected to study the effect of reaction temperature from 20 °C to 50 °C. And the percentage of $H_2O_2$ that decomposed at 20 °C, 35 °C and 50 °C was found to be 84.4%, 97.5% and 99.4%, respectively. In other words, the catalytic efficiency of the catalyst increased progressively with increasing the reaction temperatures. Because of increasing the reaction temperature accelerates the kinetics of $H_2O_2$ decomposition [67].

Furthermore, the pseudo first order rate constants were calculated from Eq. (3)

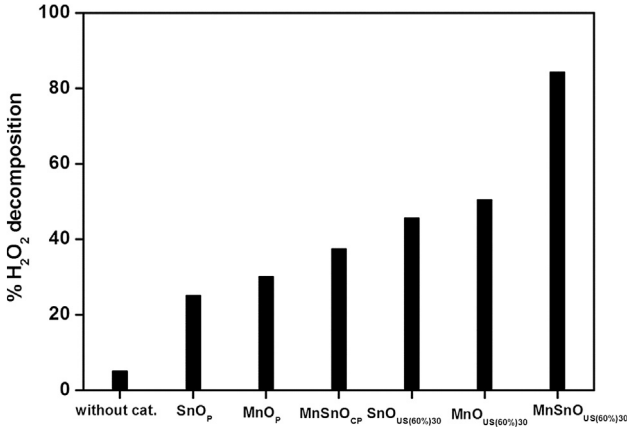


**Fig. 4.** The catalytic efficiency for decomposition of hydrogen peroxide ($H_2O_2$) in presence of $SnO_P$, $MnO_P$, $MnSnO_{CP}$, $SnO_{US(60\%)30}$, $MnO_{US(60\%)30}$, $MnSnO_{US(60\%)30}$ catalysts and without catalyst.

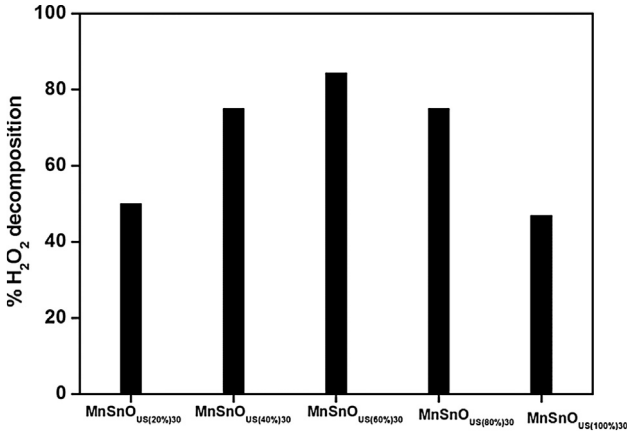


**Fig. 5.** The effect of different sonication power of $MnO_2$/$SnO_2$ catalysts on decomposition of hydrogen peroxide ($H_2O_2$).

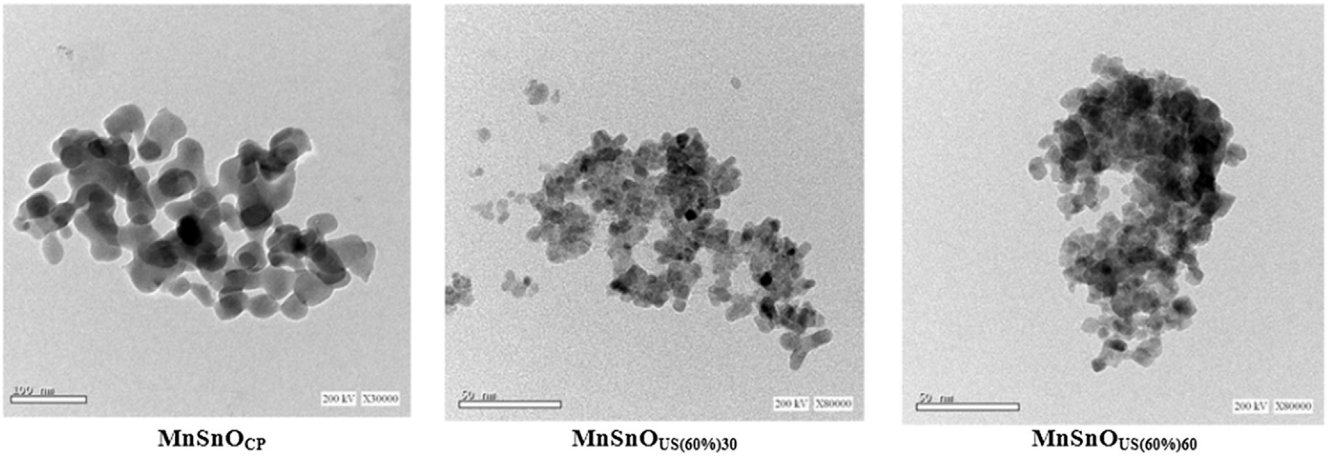


**Fig. 3.** HR-TEM images of $MnSnO_{CP}$, $MnSnO_{US(60\%)30}$ and $MnSnO_{US(60\%)60}$ catalysts calcined at 500 °C.

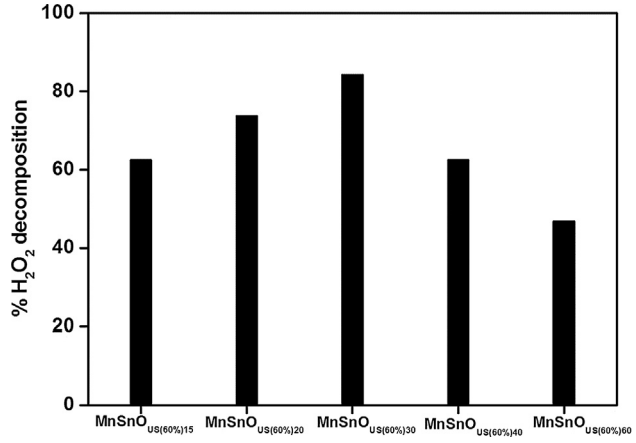


**Fig. 6.** The effect of different sonication time of $MnO_2/SnO_2$ catalysts on decomposition of hydrogen peroxide ($H_2O_2$).

$$-\ln(1-X) = kt \quad (3)$$

where k is the rate constant of reaction in $min^{-1}$, X is the value of $H_2O_2$ that decomposed by the catalyst at time t. The corresponding graphs of $-\ln(1-X)$ against t for $MnSnO_{US(60\%)30}$ catalyst at various reaction temperatures were given in Fig. 7. All graphs showed linear nature with correlation coefficient ($R^2$) higher than 0.99 that supported the reaction followed pseudo first order kinetics. It was observed that the reaction rate constant increases by increasing the temperature. However, the pseudo first order rate constants from these graphs were found to be 0.038 $min^{-1}$ at 20 °C, 0.073 $min^{-1}$ at 35 °C and 0.105 $min^{-1}$ at 50 °C. Furthermore, the activation energy which obtained for the catalytic decomposition of $H_2O_2$ using the most active catalyst was calculated from Arrhenius Eq. (4).

$$\ln k = -E_a/RT + \ln A \quad (4)$$

where $E_a$ was activation energy (J/mol), T the absolute temperature (K), A the pre-exponential factor ($min^{-1}$) and R the gas constant (8.314 J/mol K). The graph of ln k against 1/T was presented in Fig. 8, and the values of $E_a$ and A from this graph was found to be 26.7 kJ/mol and $2.3 \times 10^3$ $min^{-1}$, respectively.

### 3.4.5. Reusability and stability of $MnSnO_{US(60\%)30}$ catalyst

For industrial purposes the reusability and stability of the catalyst play a significant role. To evaluate the stability of the most active catalyst ($MnSnO_{US(60\%)30}$) was reused in four consecutive $H_2O_2$ decomposition runs at 20 °C as represented in Fig. 9. After each run, the catalyst was filtered, washed, dried and then reused with a fresh $H_2O_2$ solution. It was evident that there is no significant decrease in catalytic efficiency even after four consecutive runs. In other words, the catalytic efficiency on $MnSnO_{US(60\%)30}$ was found to be 84.4% (Fresh), 83.8% (1st reuse), 83.1% (2nd reuse), 82.3% (3rd reuse) and 81.5% (4th reuse) %, respectively. This obviously refers that the mesoporous $MnO_2/SnO_2$ catalyst sonicated at power of 60% for 30 min has high stability and catalytic efficiency for $H_2O_2$ decomposition.

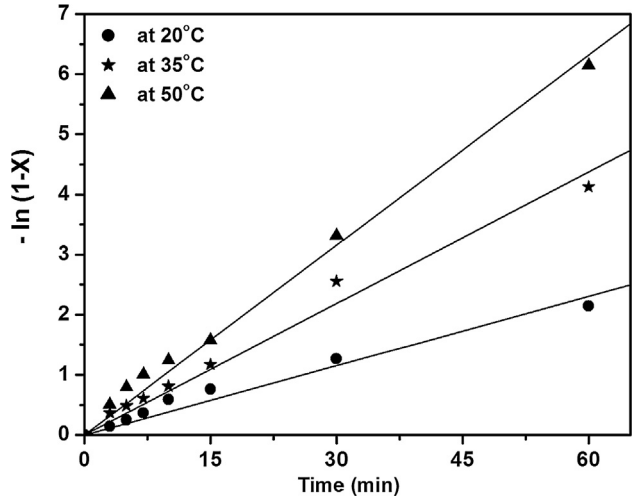


**Fig. 7.** First-order plots of $H_2O_2$ decomposition on $MnSnO_{US(60\%)30}$ catalyst at various reaction temperatures.

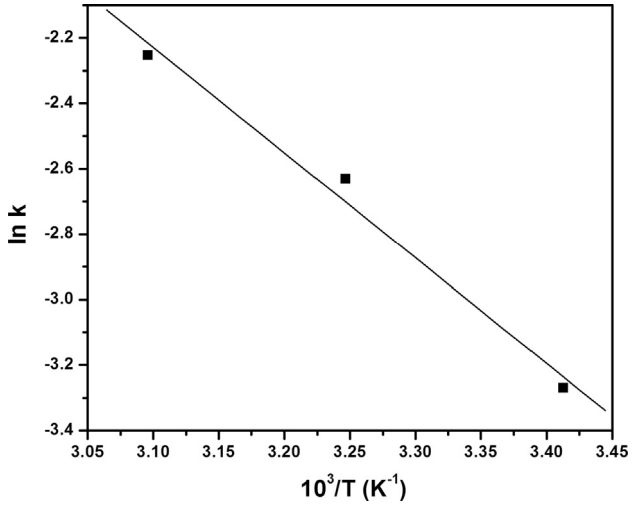


**Fig. 8.** Arrhenius plots for the decomposition of $H_2O_2$ over $MnSnO_{US(60\%)30}$ catalyst.

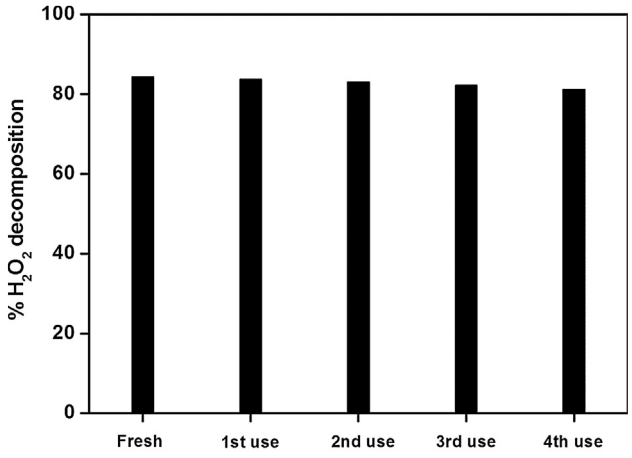


**Fig. 9.** The reusability of $MnSnO_{US(60\%)30}$ catalyst towards decomposition of $H_2O_2$.

### 3.4.6. Mechanistic explanation of $H_2O_2$ decomposition

It had been reported that the mechanism related to the decomposition of $H_2O_2$ was extremely complex [31,68–70]. The most possible reaction passage of catalytic decomposition of $H_2O_2$ was represented in Eqs. (5)–(9) [13,71]. First, the $H_2O_2$ molecule was adsorbed on the catalyst surface sites [72]. Then, the reaction beginning with electron exchange (Eq. (5)) between the $H_2O_2$ molecule and metal oxides, wherever a perhydroxyl radical ($HO_2^{\cdot}$) was created in the process [73]. The next step includes chain propagation, wherever hydroxyl radical ($HO^{\cdot}$) (Eq. (6)) and supplemental $HO_2^{\cdot}$ were created (Eq. (7)). At final step the catalyst was refilled (Eq. (8)).

$$M^{n+} + H_2O_2 \rightarrow H^+ + M^{n-1} + HO_2^{\cdot} \quad (5)$$

$$HO_2^{\cdot} + H_2O_2 \rightarrow H_2O + O_2 + HO^{\cdot} \quad (6)$$

$$HO^{\cdot} + H_2O_2 \rightarrow H_2O + HO_2^{\cdot} \quad (7)$$

$$HO^{\cdot} + M^{n-1} \rightarrow M^{n+} + OH^{-} \quad (8)$$

Moreover, a water molecule was created as the reproduction of the reaction between a hydroxide and a hydrogen ion as seen in Eq. (9).

$$H^{+} + OH^{-} \rightarrow H_2O \quad (9)$$

The reaction in Eq. (5) denotes a variation in the oxidation state of the metal ion from $M^{n+}$ to $M^{n-1}$, as was shown in several literatures [56,68,71].

## 4. Conclusions

In conclusion, novel mesoporous $MnO_2/SnO_2$ catalysts were successfully synthesized by traditional and ultrasonic co-precipitation routes. The catalytic efficiency for $H_2O_2$ decomposition of mixed oxides $MnO_2/SnO_2$ either prepared by traditional or ultrasonic co-precipitation method was greater than that of single oxides catalysts. Furthermore, the percentage of $H_2O_2$ that decomposed by $MnO_2/SnO_2$ catalyst which sonicated at power of 60% after 30 min as optimum conditions was found to be 84.4%. Additionally, the mesoporous $MnSnO_{US(60\%)30}$ catalyst had the highest BET surface area and smallest average particle diameter.

## Appendix A. Supplementary material

Supplementary data to this article can be found online at https://doi.org/10.1016/j.ultras.2019.03.011.

## References


[1] N. Tsolekile, S. Parani, M.C. Matoetoe, S.P. Songca, O.S. Oluwafemi, Evolution of ternary I-III–VI QDs: synthesis, characterization and application, Nano-Struct. Nano-Objects 12 (2017) 46–56.

[2] N. Arsalani, A. Akbari, M. Amini, E. Jabbari, S. Gautam, K.H. Chae, POSS-based Co networks: supporting and stabilizing Pd for heck reaction in aqueous media, Catal. Lett. 147 (2017) 1086–1094.

[3] A. Akbari, M. Amini, A. Tarassoli, B. Eftekhari-Sis, N. Ghasemian, E. Jabbari, Transition metal oxide nanoparticles as efficient catalysts in oxidation reactions, Nano-Struct. Nano-Objects 14 (2018) 19–48.

[4] V.P. Sharma, U. Sharma, M. Chattopadhyay, V.N. Shuklad, Advance applications of nanomaterials: a review, Mater. Today: Proc. 5 (2018) 6376–6380.

[5] J. Tian, J. Xu, F. Zhu, T. Lu, C. Su, G. Ouyang, Application of nanomaterials in sample preparation, J. Chromatogr. A 1300 (2013) 2–16.

[6] H. Osgood, S.V. Devaguptapu, H. Xu, J. Cho, G. Wu, Transition metal (Fe Co, Ni, and Mn) oxides for oxygen reduction and evolution bifunctional catalysts in alkaline media, Nano Today 11 (2016) 601–625.

[7] V. Polshettiwar, B. Baruwati, R.S. Varma, Self-assembly of metal oxides into three-dimensional nanostructures: synthesis and application in catalysis, ACS Nano 3 (2009) 728–736.

[8] M.M. Najafpour, M. Amini, M. Ashrafi, Lessons from metal oxides to find why nature selected manganese and calcium for water oxidation, Int. J. Hydrogen Energy 42 (2017) 8539–8544.

[9] J. Li, L. Li, W. Cheng, F. Wu, X. Lu, Z. Li, Controlled synthesis of diverse manganese oxide-based catalysts for complete oxidation of toluene and carbon monoxide, Chem. Eng. J. 244 (2014) 59–67.

[10] Z. Wang, D. Yang, T.-K. Sham, Effect of oxidation state of manganese in manganese oxide thin films on their capacitance performances, Surf. Sci. 676 (2018) 71–76.

[11] X. Lu, T. Zhai, X. Zhang, Y. Shen, L. Yuan, B. Hu, L. Gong, J. Chen, Y. Gao, J. Zhou, Y. Tong, Z.L. Wang, $WO_{3-x}$@Au@$MnO_2$ core-shell nanowires on carbon fabric for high-performance flexible supercapacitors, Adv. Mater. 24 (2012) 938–944.

[12] Y. Zhang, Y. Mo, Preparation of $MnO_2$ electrodes coated by Sb-doped $SnO_2$ and their effect on electrochemical performance for supercapacitor, Electrochim. Acta 142 (2014) 76–83.

[13] Z.B. Jildeh, J. Oberländer, P. Kirchner, P.H. Wagner, M.J. Schöning, Thermocatalytic behavior of manganese (IV) oxide as nanoporous material on the dissociation of a gas mixture containing hydrogen peroxide, Nanomaterials 8 (2018) 262.

[14] J. Deng, Y. Ge, C. Tan, H. Wang, Q. Li, S. Zhou, K. Zhang, Degradation of ciprofloxacin using α-$MnO_2$ activated peroxymonosulfate process: effect of water constituents, degradation intermediates and toxicity evaluation, Chem. Eng. J. 330 (2017) 1390–1400.

[15] R. Barik, N. Devi, D. Nandi, S. Siwal, S.K. Ghosh, K. Mallick, Multifunctional performance of nanocrystalline tin oxide, J. Alloy Compd. 723 (2017) 201–207.

[16] A. Huda, C.T. Handoko, M.D. Bustan, B. Yudono, F. Gulo, New route in the synthesis of Tin (II) oxide micro-sheets and its thermal transformation, Mater. Lett. 211 (2018) 293–295.

[17] S. Gnanam, V. Rajendran, Luminescence properties of EG-assisted $SnO_2$ by sol–gel process, J. Nano Mater. Bios. 5 (2010) 699–704.

[18] W.W. Wang, Y.J. Zhu, L.X. Yang, ZnO-$SnO_2$ hollow spheres and hierarchical nanosheets: hydrothermal preparation, formation mechanism, and photocatalytic properties, Adv. Funct. Mater. 17 (2007) 59–64.

[19] H.R. Mahmoud, Highly dispersed $Cr_2O_3$–$ZrO_2$ binary oxide nanomaterials as novel catalysts for ethanol conversion, J. Mol. Catal. A 392 (2014) 216–222.

[20] H.R. Mahmoud, Novel mesoporous $Gd^{3+}$ doped $Cr_2O_3$ nanomaterials: synthesis, characterization, catalytic and antitumor applications, Adv. Powder Technol. 27 (2016) 1446–1452.

[21] D.M. Clifford, C.E. Castano, J.V. Rojas, Supported transition metal nanomaterials: nanocomposites synthesized by ionizing radiation, Radiat. Phys. Chem. 132 (2017) 52–64.

[22] X. Zhao, F. Zhang, S. Xu, D.G. Evans, X. Duan, From layered double hydroxides to ZnO-based mixed metal oxides by thermal decomposition: transformation mechanism and uv-blocking properties of the product, Chem. Mater. 22 (2010) 3933–3942.

[23] L. Gu, L. Qian, Y. Lei, Y. Wang, J. Li, H. Yuan, D. Xiao, Microwave-assisted synthesis of nanosphere-like $NiCo_2O_4$ consisting of porous nanosheets and its application in electro-catalytic oxidation of methanol, J. Power Sources 261 (2014) 317–323.

[24] J.R. Kim, K.Y. Lee, M.J. Suh, S.K. Ihm, Ceria-zirconia mixed oxide prepared by continuous hydrothermal synthesis in supercritical water as catalyst support, Catal. Today 185 (2012) 25–34.

[25] L.I. Nadaf, K.S. Venkatesh, Synthesis and characterization of tin oxide nanoparticles by co-precipitation method, J. Appl. Chem. 9 (2016) 1–4.

[26] J.Y. Lee, W.-K. Jo, Application of ultrasound-aided method for the synthesis of CdS-incorporated three-dimensional $TiO_2$ photocatalysts with enhanced performance, Ultrason. Sonochem. 35 (2017) 440–448.

[27] X. Ma, Y. Cheng, Y. Ge, H. Wu, Q. Li, N. Gao, J. Deng, Ultrasound-enhanced nanosized zero-valent copper activation of hydrogen peroxide for the degradation of norfloxacin, Ultrason. Sonochem. 40 (2018) 763–772.

[28] N. Zhang, G. Zhang, S. Chong, H. Zhao, T. Huang, J. Zhu, Ultrasonic impregnation of $MnO_2/CeO_2$ and its application in catalytic sono-degradation of methyl orange, J. Environ. Manage. 205 (2018) 134–141.

[29] B. Tamami, S. Ghasemi, Catalytic activity of Schiff-base transition metal complexes supported on crosslinked polyacrylamides for hydrogen peroxide decomposition, J. Organomet. Chem. 794 (2015) 311–317.

[30] J.H. Chi, S.H. Wu, J.C. Charpentier, C.M. Shu, Thermal hazard accident investigation of hydrogen peroxide mixing with propanone employing calorimetric approaches, J. Loss. Prev. Process Ind. 25 (2012) 142–147.

[31] R. Ribeiro, A.M.T. Silva, J.L. Figueiredo, J.L. Faria, H.T. Gomes, The influence of structure and surface chemistry of carbon materials on the decomposition of hydrogen peroxide, Carbon 62 (2013) 97–108.

[32] Y. Batonneau, C. Kappenstein, W. Keim, in: G. Ertl, H. Knöinger, F. Schüth, J. Weitkamp (Eds.), Handbook of Heterogeneous Catalysis, vol. 5, second ed., VCH Wiley, Weinheim, 2008 (Chapter 12.7).

[33] M.I. Zaki, A. Katrib, A.I. Muftah, T.C. Jagadale, M. Ikram, S.B. Ogale, Exploring anatase- $TiO_2$ doped dilutely with transition metal ions as nano-catalyst for $H_2O_2$ decomposition: spectroscopic and kinetic studies, Appl. Catal. A 452 (2013) 214–221.

[34] A.K.H. Nohman, M.M. Mohamed, M.I. Zaki, Current topics in catalysis, Research Trends, New Delhi 4 (2005) 43–78.

[35] H.P. Klug, L.E. Alexander, X-ray Diffraction Procedures for Polycrystalline and Amorphous Materials, John Wiley and Sons, New York, 1966, p. 491.

[36] N.C. Horti, M.D. Kamatagi, N.R. Patil, M.N. Wari, S.R. Inamdar, Photoluminescence properties of $SnO_2$ nanoparticles: effect of solvents, Int. J. Light Electron Opt. 169 (2018) 314–320.

[37] D.V. Pinjari, A.B. Pandit, Room temperature synthesis of crystalline $CeO_2$ nanopowder: advantage of sonochemical method over conventional method, Ultrason. Sonochem. 18 (2011) 1118–1123.

[38] M.P. Deosarkar, S.M. Pawar, S.H. Sonawane, B.A. Bhanvase, Process intensification of uniform loading of $SnO_2$ nanoparticles on graphene oxide nanosheets using a novel ultrasound assisted in situ chemical precipitation method, Chem. Eng. Process. 70 (2013) 48–54.

[39] H. Peng, L. Zhang, Q. Sun, J. Shen, X. Xu, X. Fang, W. Liu, Z. Wang, N. Zhang, X. Wang, Facile hydrothermal synthesis of Sn-Mn mixed oxide nano-rods with exposed (110) facets and remarkable catalytic performance, Chem. Select 2 (2017) 6364–6369.

[40] H. Taguchi, K. Hirota, S. Nishihara, S. Morimoto, K. Takaoka, M. Yoshinaka, O. Yamaguchi, Effects of $Mn^{3+}$ ions on the electrical and magnetic properties of Ca$(Mn_{1-x}Zr_x)O_{3-\delta}$ ($0 \leq x \leq 0.07$), Physica B 367 (2005) 188–194.

[41] D. Mohanta, K. Barman, S. Jasimuddin, M. Ahmaruzzaman, MnO doped $SnO_2$ nanocatalysts: activation of wide band gap semiconducting nanomaterials towards visible light induced photoelectron catalytic water oxidation, J. Colloid Interf. Sci. 505 (2017) 756–762.

[42] N.S. Sabri, M.S.M. Deni, A. Zakaria, M.K. Talari, Effect of Mn doping on structural and optical properties of $SnO_2$ nanoparticles prepared by mechanochemical processing, Phys. Proc. 25 (2012) 233–239.

[43] P. Manjunathan, V.S. Marakatti, P. Chandra, A.B. Kulal, S.B. Umbarkar, R. Ravishankar, G. Anapati, V. Shanbhag, Mesoporous tin oxide: an efficient catalyst with versatile applications in acid and oxidation catalysis, Catal. Today 309 (2018) 61–76.

[44] S. Badoga, R.V. Sharma, A.K. Dalai, J. Adjaye, Synthesis and characterization of mesoporous aluminas with different pore sizes: application in NiMo supported catalyst for hydrotreating of heavy gas oil, Appl. Catal. A 489 (2015) 86–97.

[45] H.R. Mahmoud, Novel amorphous mesoporous $0.25Cr_2O_3$-$0.75ZrO_2$ nanomaterials synthesized by a surfactant-assisted hydrothermal method for ethanol oxidation, J. Alloy Compd. 687 (2016) 954–963.
[46] C. Rao, J. Shen, F. Wang, H. Peng, X. Xu, H. Zhan, X. Fang, J. Liu, W. Liu, X. Wang, $SnO_2$ promoted by alkali metal oxides for soot combustion: the effects of surface oxygen mobility and abundance on the activity, Appl. Surf. Sci. 435 (2018) 406–414.
[47] Y. Wu, Y. Lu, C. Song, Z. Ma, S. Xing, Y. Gao, A novel redox-precipitation method for the preparation of α-$MnO_2$ with a high surface $Mn^{4+}$ concentration and its activity toward complete catalytic oxidation of o-xylene, Catal. Today 201 (2013) 32–39.
[48] V.D. Mote, J.S. Dargad, B.N. Dole, Effect of Mn doping concentration on structural, morphological and optical studies of ZnO nano-particles, Nanosci. Nanoeng. 1 (2013) 116–122.
[49] M.D. Luque de Castro, F. Priego-Capote, Ultrasound-assisted crystallization (sonocrystallization), Ultrason. Sonochem. 14 (2007) 717–724.
[50] S. Askari, R. Halladj, Ultrasonic pretreatment for hydrothermal synthesis of SAPO-34 nanocrystals, Ultrason. Sonochem. 19 (2012) 554–559.
[51] A.K. Aboul-Gheit, S.M.K. Aboul-Fotouh, L.I. Ali, M.A. Naghmash, Ultrasonication of H-MoR zeolite catalysts for dimethylether (DME) production as a clean fuel, J. Pet. Technol. Altern. Fuels 5 (2014) 13–25.
[52] P.R. Gogate, V.S. Sutkar, A.B. Pandit, Sonochemical reactors: important design and scale up considerations with a special emphasis on heterogeneous systems, Chem. Eng. J. 166 (2011) 1066–1082.
[53] J. Wang, Z. Wang, C.L.Z. Vieira, J.M. Wolfson, G. Pingtian, S. Huang, Review on the treatment of organic pollutants in water by ultrasonic technology, Ultrason. Sonochem. (2019), https://doi.org/10.1016/j.ultsonch.2019.01.017 (in press).
[54] R.D.C. Soltani, M. Mashayekhi, A. Khataee, M.J. Ghanadzadeh, M. Sillanpää, Hybrid sonocatalysis/electrolysis process for intensified decomposition of amoxicillin in aqueous solution in the presence of magnesium oxide nanocatalyst, J. Ind. Eng. Chem. 64 (2018) 373–382.
[55] S. Jorfi, S. Pourfadakari, B. Kakavandi, A new approach in sono-photocatalytic degradation of recalcitrant textile wastewater using MgO@Zeolite nanostructure under UVA irradiation, Chem. Eng. J. 343 (2018) 95–107.
[56] M.A. Hasan, M.I. Zaki, L. Pasupulety, K. Kumari, Promotion of the hydrogen peroxide decomposition activity of manganese oxide catalysts, Appl. Catal. A 181 (1999) 171–179.
[57] M. Răciulete, G. Layrac, F. Papa, C. Negrilă, D. Tichit, I.-C. Marcu, Influence of Mn content on the catalytic properties of Cu-(Mn)-Zn-Mg-Al mixed oxides derived from LDH precursors in the total oxidation of methane, Catal. Today 306 (2018) 276–286.
[58] H. Yin, X. Wang, Z. Qin, M. Ginder-Vogel, S. Zhang, S. Jiang, F. Liu, S. Li, J. Zhang, Y. Wang, Coordination geometry of $Zn^{2+}$ on hexagonal turbo straticbirnes sites with different Mn average oxidation states and its stability under acid dissolution, J. Environ. Sci. 65 (2018) 282–292.
[59] J. Deng, S. Feng, X. Ma, C. Tan, H. Wang, S. Zhou, T. Zhang, J. Li, Heterogeneous degradation of Orange II with peroxymonosulfate activated by ordered mesoporous $MnFe_2O_4$, Sep. Purif. Technol. 167 (2016) 181–189.
[60] L. Zhang, L. Li, Y. Cao, Y. Xiong, S. Wu, J. Sun, C. Tang, F. Gao, L. Dong, Promotional effect of doping $SnO_2$ into $TiO_2$ over a $CeO_2$/$TiO_2$ catalyst for selective catalytic reduction of NO by $NH_3$, Catal. Sci. Technol. 5 (2015) 2188–2196.
[61] Z. Liu, X. Feng, Z. Zhou, Y. Feng, J. Li, Ce-Sn binary oxide catalyst for the selective catalytic reduction of $NO_x$ by $NH_3$, Appl. Surf. Sci. 428 (2018) 526–533.
[62] S.A. El-Molla, H.R. Mahmoud, Synthesis, textural and catalytic properties of nanosized $Fe_2O_3$/MgO system, Mater. Res. Bull. 48 (2013) 4105–4111.
[63] C. Su, W. Li, X. Liu, X. Huang, X. Yu, Fe-Mn-sepiolite as an effective heterogeneous Fenton-like catalyst for the decolorization of reactive brilliant blue, Front. Environ. Sci. Eng. 10 (2016) 37–45.
[64] L. Mei, L. Jitai, S. Hanwen, Treatment of organic pollutants in water by ultrasound, Prog. Chem. 20 (2008) 1187–1195.
[65] I.M. Mahbubul, E.B. Elcioglu, R. Saidur, Optimization of ultrasonication period for better dispersion and stability of $TiO_2$-water nanoflulid, Ultrason. Sonochem. 37 (2017) 360–367.
[66] F. Li, L. Li, G. Zhong, Y. Zhai, Z. Li, Effects of ultrasonic time, size of aggregates and temperature on the stability and viscosity of Cu-ethylene glycol (EG) nanofluids, Int. J. Heat Mass Transfer 129 (2019) 278–286.
[67] O. Zeine, B.A. Hedi, M.R. Jeday, C. Cheker, Kinetic study of the catalytic decomposition of $H_2O_2$ in phosphoric acid medium, Int. J. Hydrogen Energy 40 (2015) 1278–1282.
[68] L. Micoli, G. Bagnasco, M. Turco, M. Trifuoggi, A. Russo Sorge, E. Fanelli, P. Pernice, A. Aronne, Vapor phase $H_2O_2$ decomposition on Mn based monolithic catalysts synthesized by innovative procedures, Appl. Catal. B 140–141 (2013) 516–522.
[69] A. Aguinaco, J.P. Pocostales, J.F. García-Araya, F.J. Beltrán, Decomposition of hydrogen peroxide in the presence of activated carbons with different characteristics, J. Chem. Technol. Biotechnol. 86 (2011) 595–600.
[70] A. Rey, A. Bahamonde, J.A. Casas, J.J. Rodríguez, Selectivity of hydrogen peroxide decomposition towards hydroxyl radicals in catalytic wet peroxide oxidation (CWPO) over Fe/AC catalysts, Water Sci. Technol. 61 (2010) 2769–2778.
[71] J. Oberländer, P. Kirchner, H.G. Boyen, M.J. Schöning, Detection of hydrogen peroxide vapor by use of manganese (IV) oxide as catalyst for calorimetric gas sensors, Phys. Status Solidi A 211 (2014) 1372–1376.
[72] S.S. Lin, M.D. Gurol, Catalytic decomposition of hydrogen peroxide on iron oxide: kinetics, mechanism, and implications, Environ. Sci. Technol. 32 (1998) 1417–1423.
[73] S.H. Do, B. Batchelor, H.K. Lee, S.H. Kong, Hydrogen peroxide decomposition on manganese oxide (pyrolusite): kinetics, intermediates, and mechanism, Chemosphere 75 (2009) 8–12.